journal of the mechanical behavior of biomedical materials 113 (2021) 104130

Contents lists available at ScienceDirect

Journal of the Mechanical Behavior of Biomedical Materials

journal homepage: http://www.elsevier.com/locate/jmbbm

Mechanical behavior of *in-situ* alloyed Ti6Al4V(ELI)-3 at.% Cu lattice structures manufactured by laser powder bed fusion and designed for implant applications

A.M. Vilardell [a,*], A. Takezawa [b], A. du Plessis [c], N. Takata [d], P. Krakhmalev [a], M. Kobashi [d], M. Albu [e], G. Kothleitner [f], I. Yadroitsava [g], I. Yadroitsev [g]

[a] Karlstad University, Department of Engineering and Physics, Karlstad, SE-651 88, Sweden
[b] Dept. of Applied Mechanics and Aerospace Engineering, School of Fundamental Science and Engineering, Waseda University, 59-311, 3-4-1 Okubo, Shinjuku-ku, Tokyo, 169-8555, Japan
[c] Research Group 3D Innovation, Stellenbosch University, Stellenbosch, 7602, South Africa
[d] Dept. of Materials Process Engineering, Graduate School of Engineering, Nagoya University, Furo-cho, Chikusa-ku, Nagoya, 464-8603, Japan
[e] Graz Centre for Electron Microscopy (ZFE), Steyrergasse 17-3, A-8010, Graz, Austria
[f] Institute of Electron Microscopy and Nanoanalysis, Graz University of Technology, Steyrergasse 17-3, A-8010, Graz, Austria
[g] Dept. of Mechanical and Mechatronics Engineering, Central University of Technology, Bloemfontein, 9300, South Africa

ARTICLE INFO

Keywords:
Cellular lattice structures
Laser powder bed fusion
Ti6Al4V(ELI)-Cu
Mechanical properties
In-situ alloying

ABSTRACT

In the present study, cellular lattice structures for implant applications are reported for the first-time incorporating copper directly by *in-situ* alloying in the laser powder bed fusion process. The aim to incorporate 3 at.% Cu into Ti6Al4V(ELI) is selected for improved antibacterial properties while maintaining appropriate mechanical properties. Previously, topologically optimized Ti6Al4V(ELI) lattice structures were successfully designed, manufactured and studied for implant applications. The development of a new alloy produced by *in-situ* alloying of elemental powder mixture of Ti6Al4V(ELI) and pure Cu powders was used here for the production of identical lattice structures with improved antibacterial properties. One of the same as-designed CAD models was used for the manufacturing of these lattices compared to previous work on pure Ti6Al4V(ELI) lattices, making direct comparison of mechanical properties possible. Similar manufacturability highlights the applicability of this alloying technique to other lattice designs. Microstructural characterization was performed by optical and electron microscopies, as well as microCT. Mechanical characterization was performed by means of compression tests and hardness measurements. Results showed that *in-situ* alloying with copper leads to the formation of localized Cu-rich regions, refinement of martensitic phase and the formation of $CuTi_2$ intermetallic precipitates, which increased the hardness and strength of the material. Deviations in wall thickness between the as-designed and as-manufactured lattices led to anisotropy of the mechanical properties of the lattices. Higher compressive strength values were obtained when thicker walls were oriented along the loading direction. Nevertheless, alloying with Cu had a higher impact on the compressive strength of lattice structure than the wall thickness deviations. The direct *in-situ* alloying of copper in Ti6Al4V(ELI) is a promising route for direct manufacturing of antibacterial implants.

1. Introduction

Laser powder bed fusion (L-PBF) is an additive manufacturing process that allows freedom in design, which is beneficial for the manufacturing of complex geometries, e.g. cellular lattice structures (CLS). Briefly, a laser beam scans and irradiates a powder bed, which selectively melts the powder, layer by layer until a 3D part is manufactured. Geometrical and structural factors of CLS such as connectivity, pore size and relative density are important for the design of implant prostheses with suitable mechanical and biological properties (Maconachie et al., 2019). Light-weight Ti6Al4V CLS allows the decrease in effective elastic modulus closer to the human bone, thus being beneficial

* Corresponding author.
E-mail address: amvilardell.research@gmail.com (A.M. Vilardell).

https://doi.org/10.1016/j.jmbbm.2020.104130
Received 18 August 2020; Received in revised form 22 September 2020; Accepted 1 October 2020
Available online 5 October 2020

by decreasing/avoiding stress shielding and promoting bone in-growth (Yánez et al., 2016; Onal et al., 2018). Therefore, the increase in porosity of such lattices is desired for favorable permeability of mass/-fluid transport (Zhang et al., 2019), although a smaller pore size (300–400 μm) has been found to be more suitable than bigger ones (400–500 μm and 500–700 μm) for cell adhesion and proliferation (Li et al., 2016). Recently, different approaches for CLS design, such as CAD-based and image-based, have arisen to merge the structural and mechanical needs for implant prostheses with desired relative density/porosity, as well as effective elastic modulus (Xu et al., 2019; Vilardell et al., 2019). Therefore, theoretical and experimental analyses demonstrated the possibility to vary such architectural features without dramatically altering the mechanical performance of the structure (Maietta et al., 2019).

Lately, *in-situ* alloying of mixed elemental powders by L-PBF have shown its benefits to produce new materials with unique properties in an economic way compared to prealloyed powder. Within the biomedical field, the *in-situ* alloying of Ti alloys with β-stabilizer elements such as molybdenum (Mo) (Kang et al., 2019), tantalum (Ta) (Huang et al., 2020) and niobium (Nb) (Fischer et al., 2016) are of high interest to reduce the elastic modulus. Dense Ti7.5wt.%Mo (over 99.5%) has been obtained with an elastic modulus ~70 GPa (Kang et al., 2019), compared to the elastic modulus of commercial pure titanium (E~120 GPa). Therefore, dense Ti10wt.%Ta, Ti30wt.%Ta and Ti50wt.%Ta (over 99.5%) have been successfully manufactured by L-PBF. Yield and ultimate strengths increased up to 30 wt.% Ta meanwhile elastic modulus reduced down to 70 GPa. Higher content of Ta (Ti50wt.%Ta) results in a drop of strength caused by the formation of β (BCC) phase which exhibits more slip systems (Huang et al., 2020). For *in-situ* L-PBF Ti26at.%Nb alloy, lower elastic modulus has been obtained too (E~77 GPa), with porosity content inferior to 3% (Fischer et al., 2016). On the other hand, *in-situ* alloying of Ti alloys by L-PBF with antibacterial elements, such as Cu, is promising. Infected prostheses are hard to treat with antibiotic therapy since bacteria biofilm-correlated infections are highly resistant to antibiotic treatments and also to the host immune response (Song et al., 2013). The bactericidal effect of *in-situ* alloying L-PBF Ti6Al4V-1 at.% Cu has been demonstrated (Krakhmalev et al., 2017). The increase in Cu leads to an increase in bactericidal effect (Ren et al., 2014). However, lower amounts of Cu (~5 wt.%) are recommended to ensure a good bactericidal effect without toxicity and without modifying significantly the final mechanical properties of the titanium alloy (Liu et al., 2014; Peng et al., 2019).

The novelty and originality of this research is the combination of topology optimized CLS, with a relative density and effective elastic modulus close to the human bone, together with the bactericidal effect provided by the *in-situ* alloying of pure Cu with pure Ti6Al4V(ELI) elemental powders by L-PBF. The novel combination of Ti6Al4V(ELI) CLS together with the addition of copper content would provide enhanced osteointegration, reduce the effects of stress shielding, and minimize the risk of bacterial infection. For that purpose, topology optimized Ti6Al4V(ELI) CLS with a relative density of 45% and a corresponding effective elastic modulus of 18.6 GPa from a previous study (Vilardell et al., 2019), were selected to be *in-situ* alloyed manufactured with 3 at.% Cu (Vilardell et al., 2020). Thus, the goal of this research is the manufacturing and mechanical characterization of *in-situ* alloyed Ti6Al4V(ELI) −3 at.% Cu CLS designed for biomedical applications by L-PBF.

2. Materials and experimental methods

2.1. Feedstock powder

Argon gas atomized Ti6Al4V(ELI) and Cu feedstock powders with spherical morphologies supplied by TLS Technik GmbH & Co. Spezialpulver KG (Germany) were used in this study. The chemical composition of Ti6Al4V(ELI) powder was of 89.26 wt% Ti, 6.31 wt% Al, 4.09 wt% V, 0.12 wt% O. The Cu powder had a purity of 99.9%. The particle size distribution of both powders were similar: $Ø_{10} = 12.6$ μm, $Ø_{50} = 22.9$ μm, $Ø_{90} = 37.0$ μm, for the Ti6AlV(ELI) powder, and $Ø_{10} = 9.45$ μm, $Ø_{50} = 21.9$ μm, $Ø_{90} = 37.5$ μm for Cu powder (weighted by volume). The Ti6Al4V(ELI)- 3 at.% Cu powder mixture was made by mixing powders for 1 h by continuously manually inverting a metal container. The final powder mixture was dried at 80 °C for 2 h before manufacturing. Elemental powders were chosen for the present study since these are already available in the market and provide a more flexible and economical manufacturing, compared to pre-alloyed ones.

2.2. Laser power bed fusion process

In a previous study (Vilardell et al., 2019), a topology optimization approach was used for the design of Ti6Al4V(ELI) cellular lattice structures with stiffness and density close to human bone for implant applications. Three lattice designs with volume densities of 35%, 40% and 45% and corresponding effective elastic modulus of 18.6 GPa, 23.1 GPa 27.4 GPa were obtained. The CLS consisted of the repetition ($7 \times 7 \times 7$ along X, Y and Z directions) of a topology optimized unit cell. In the present study, the CLS design with 45% volume density was chosen to be *in-situ* alloyed by L-PBF Ti6Al4V(ELI) - 3 at.% Cu. The selected lattices were produced by EOSINT M280 system (EOS GmbH) at 30 μm powder layer thickness. A laser power of 170 W, scanning speed of 0.7 m/s and hatch distance of 80 μm was chosen for the manufacturing of the *in-situ* alloyed L-PBF Ti6Al4V(ELI) – 3 at.% Cu CLS. The optimization process and parameters of this material were studied in detail for solid single tracks, layers and cubes in (Vilardell et al., 2020). The manufacturing process was performed under Argon (Ar) atmosphere, and the oxygen level was controlled (<0.07%). Eight CLS with dimensions of $20 \times 20 \times 20$ mm^3 were manufactured directly on the Ti6Al4V base plate without supports. Later on, a stress-relief treatment was performed in Ar atmosphere at 650 °C for 3 h before the specimens were cut off from the base plate using wire electrical discharge machining.

2.3. Physical and microstructural measurements

L-PBF Ti6Al4V(ELI) −3 at.% Cu CLS were investigated by scanning electron microscopy (SEM) LEO 1350 FEG, operated at 20 kV. The cross-sections were prepared by grinding and polishing procedures until mirror-like finish was achieved with colloidal silica. Later on, samples were etched in Kroll's reagent. SEM and optical (Leica DMI 3000 M) microscopies were used for microstructural analyses. X-ray diffraction (XRD- Ultima IV, Rigaku) measurements were conducted using a Cu-Kα radiation source (wave length $\lambda = 0.15405$ nm) operated at 40 kV and 40 mA to identify constituent phases. The electron backscatter diffraction (EBSD) analyses were performed using FE-SEM (JEOL JSM-7000 F) operated at 20 kV. The scan analyses were carried out at step sizes of 0.2 and 0.3 μm using the material data of α-Ti (hcp) and β-Ti (bcc) phases for preparing the phase distribution maps. Thin slices of $10 \times 7 \times 1$ mm^3 in size were cut and ion-polished by a JEOL cross-section polisher at 6 V for EBSD examination. Additionally, high-resolution scanning transmission electron microscopy (HR-STEM) was performed by using a FEI Titan 3 G2 60–300 STEM equipped with a Cs corrector operated at 300 keV. HR-STEM microscope was equipped with a Super X detector (4 Si-drift detectors) for chemical analyses by x-ray spectroscopy. Element mapping was acquired and processed with VELOX software (Schlossmacher et al., 2010). HR-STEM sample was prepared by argon ion-milling at room temperature.

X-ray microCT was used for analysis of the produced samples. The system used in this work was a General Electric Vtomex L240, with image analysis performed using Volume Graphics VGStudio Max 3.2 (du Plessis et al., 2016). The designed porosity and walls' microporosity were analysed using identical settings as those in the previous study of Ti6Al4V (ELI) CLS (Vilardell et al., 2019), at 25 μm voxel size. Wall thickness measurements were made linearly at the thinnest part of the

walls found by microCT cross-sections. Additionally, higher resolution microCT scans were performed on small CLS sections of 5 × 5 × 5 mm^3 at 5 μm voxel size. This allowed wall microporosity to be measured with a minimum pore diameter of about 15 μm. The latter scans were performed with a General Electric Nanotom S system.

2.4. Mechanical characterization

Uniaxial compression test of the CLS were performed according to ISO 13314 (ISSO 13314 - Mechanical testing of metals, 1331), using a TokyoKoki Seizosho mechanical testing machine (Japan) with a loading cell capacity of 50 tons. Samples were placed between the crossheads of the testing machine. Before running the tests, a standard preload was applied to ensure the contact between the crossheads and the specimen. The displacement rate of the crossheads was set to 1.5 mm/s. The strain of the sample was measured by the actual displacement of the crossheads of the testing machine recorded with a Data logger NR-600 (Keyence) until the sample completely collapsed. Three specimens were tested for each orientation, parallel and perpendicular to the L-PBF building direction. This was important as the thickness of vertical/parallel and horizontal/perpendicular lattice walls were different due to the L-PBF process. Vickers hardness was measured with a LECO V-100-C2 hardness tester on the polished cross-sections. The load was 200 g and the load time was 15 s. At least 30 measurements for each cross-section were done.

3. Results

3.1. Physical measurements

The topology optimized cubic unit cell (2.857 mm each direction, Fig. 1a) was replicated 7 times in X, Y and Z directions (Fig. 1b). Fig. 1c shows the *in-situ* alloyed Ti6Al4V(ELI)-3 at.% Cu CLS. Fig. 2 illustrates SEM micrographs of Ti6Al4(ELI)- 3 at.% Cu of the free surface of horizontal and vertical walls corresponding to perpendicular/horizontal (PER/HOR) and parallel/vertical (PAR/VER) walls relative to the building direction (BD). The difference in wall thicknesses was observed where horizontal walls were much thicker than the vertical walls. As-manufactured specimens showed thinner vertical and thicker horizontal wall thicknesses in comparison with the as-designed model for both materials (Fig. 2). Table 1 shows the wall thickness and porosity values of as-design and as-manufactured Ti6Al4V(ELI)-3 at.% Cu CLS in comparison with the previously reported Ti6Al4V(ELI) CLS (Vilardell et al., 2019). Vertical and horizontal walls of Ti6Al4V(ELI)-3 at.% Cu CLS were 31% thinner and 75% thicker compared to the as-designed ones, respectively. The same trend was found in our previous work of Ti6Al4V (ELI) CLS, although wall thickness deviations were lower compared to Ti6Al4V(ELI)-3 at.% Cu CLS. The porosity values of the L-PBF Ti6Al4V (ELI)-3 at.% Cu and Ti6Al4V(ELI) CLS were 6.5vol.% and 11.5vol.% respectively higher than the as-designed one. The discrepancies in the minimum wall thickness mainly led to the increase in the CLS porosity.

Ti6Al4V(ELI)-3 at.% Cu CLS were cut in small pieces to analyze at high resolution the microporosity of the walls by microCT. Fig. 3a and b

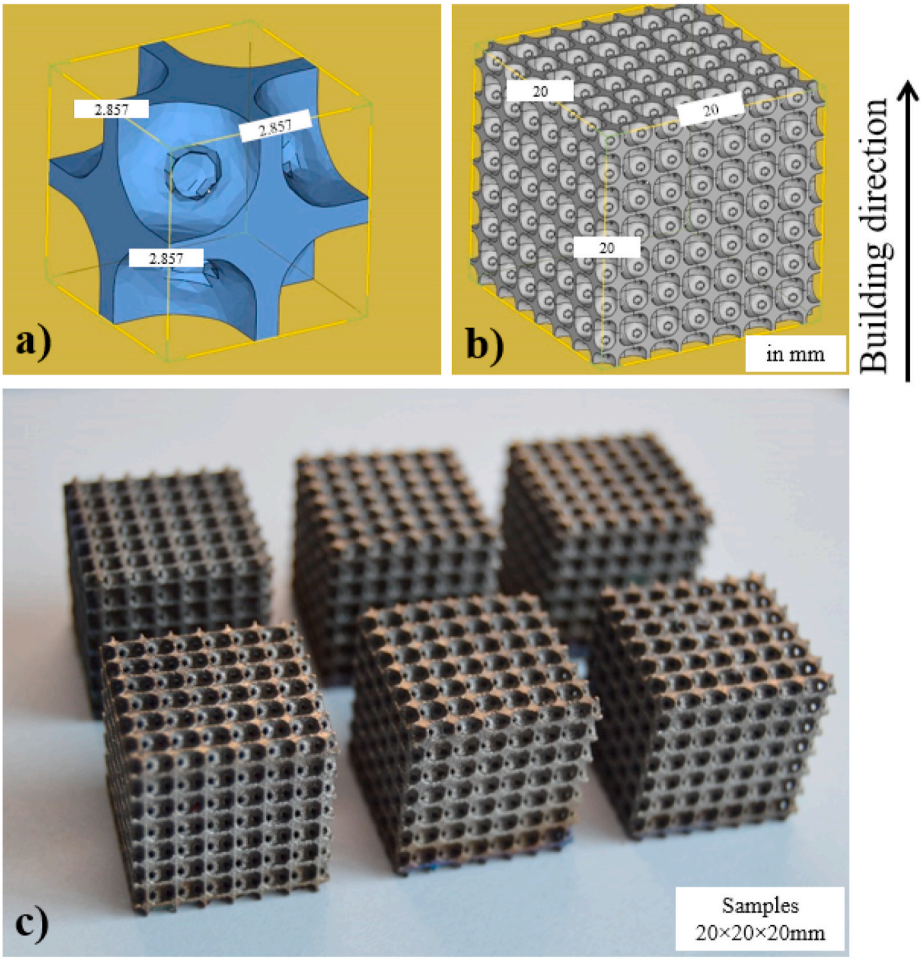

Fig. 1. (a) A cell unit, and (b) CLS after its repetition 7 times in X,Y, Z directions and after being rescaled down to 20 × 20 × 20 mm^3 (Vilardell et al., 2019); (c) L-PBF Ti6Al4V(ELI)-3 at.% Cu specimens.

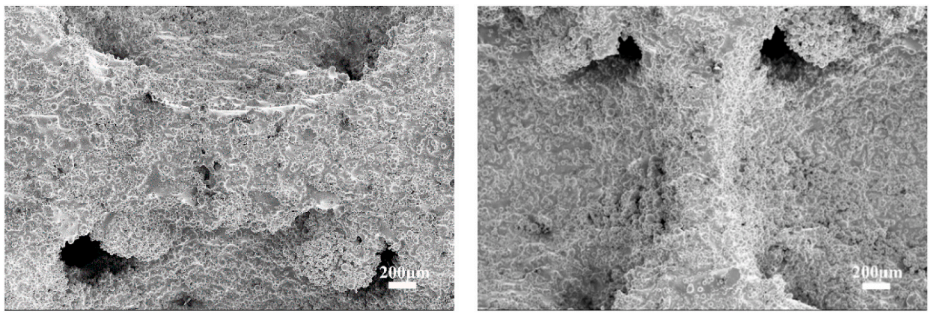

Fig. 2. SEM micrographs of (a) HOR and (b) VER walls of L-PBF Ti6Al4V(ELI)-3 at.% Cu CLS.

Table 1
Wall thickness and porosity values of L-PBF Ti6Al4V(ELI)-3 at.% Cu and Ti6Al4V(ELI) CLS.

	Ti6Al4V(ELI)-3 at.% Cu CLS	Ti6Al4V(ELI) CLS (Vilardell et al., 2019)
As-designed wall thickness [μm]		349
MicroCT measured thickness [μm]-*Vertical walls*	239.2 ± 50	192.1 ± 14
MicroCT measured thickness [μm]-*Horizontal walls*	610.3 ± 25.8	470.6 ± 36.9
As-designed porosity [vol.%]		56.2
MicroCT measured porosity [vol.%]	59.9 ± 2.9	62.7 ± 0.003

show the 3D microCT scan and its cross-section, respectively. The inner porosity and enriched Cu areas on the surface of the CLS can be observed in Fig. 3b (brighter colour). Although microCT does not provide chemical analysis, enriched Cu areas can be distinguished in microCT scans since these areas are more x-ray dense than surrounding material, indicating a heavier metal than Ti6Al4V(ELI). Such particles were found in this material but not in Ti6AlV(ELI) without copper under the same process conditions (Vilardell et al., 2019). Previous SEM/EDS investigation of *in-situ* alloyed Ti6Al4V(ELI)-3 at.% Cu confirmed the presence of such enriched Cu areas (Vilardell et al., 2020). Microporosity measurements of Ti6Al4V(ELI)-3 at.% Cu material showed a value of 0.40 ± 0.06 vol.%, a bit higher compared to 0.12 ± 0.04 vol.% of Ti6Al4V(ELI) material (Vilardell et al., 2019). The addition of 3 at.% Cu also showed larger pores, distributed evenly within the CLS. A significant number of pores between a range of 95–180 μm, much larger in comparison with pores below 45.3 μm of Ti6Al4V(ELI) CLS (Vilardell et al., 2019).

3.2. Microstructural analyses

L-PBF Ti6Al4V(ELI)-3 at.% Cu consisted of a fine acicular α′ martensite phase microstructure where columnar prior β-grains parallel to the BD up to several millimetres in length (Fig. 4a). Microporosity was observed agreeing with the presented microCT results. Higher magnification SEM micrograph shows that homogenization was hard to achieve by showing Cu-rich areas. Copper measurements by EDX method at the fusion boundaries was between 9.5 and 10.5 wt.% (Fig. 4b). Fig. 4c shows the EBSD phase mapping showing a finer microstructure compared to L-PBF Ti6Al4V(ELI) (Vilardell et al., 2019). A small percentage of β-phase (Fig. 4c, green colour) was observed and spotted between α' martensite needles (Fig. 4c, red colour). Additionally, rounded α grains within of a size about 10 μm were found within the microstructure, which likely can be associated to α-phase due to its hcp structure but also rounded shape (Fig. 4c – white arrows). XRD results confirm the presence of α/α′ phase, as well as β-phase due to the increase in intensity of overlapped α/α' and β phases when comparing with Ti6Al4V(ELI) material (Fig. 4d). In addition, a couple of diffractions derived from an intermetallic $CuTi_2$ phase were detected (Fig. 4d).

The formation of α and β phases can be explained by the thermocycling process of L-PBF or the stress-relief treatment, leading the transformation of α'-phase into α and β phases (Xu et al., 2015; Sallica-Leva et al., 2016). Additionally, it should be noticed that Ti6Al4V(ELI)-3 at.% Cu showed higher amount of β-phase than Ti6Al4V(ELI) material (Vilardell et al., 2019), probably due to the addition of Cu as a β-phase stabilizer. Although the material data of tetragonal $CuTi_2$ phase was not applied in the present EBSD analyses (Fig. 4c), HR-STEM confirmed its presence (Fig. 5). The precipitates of $CuTi_2$ intermetallic phase (with Cu-rich and V-poor composition) were preferentially observed at the

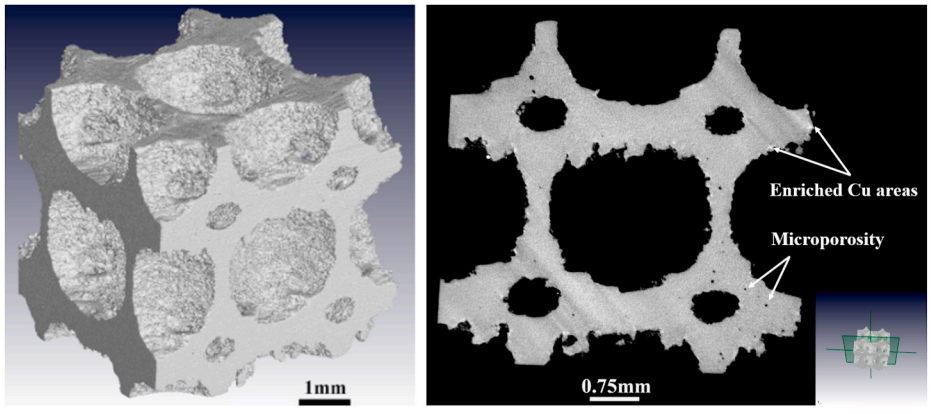

Fig. 3. MicroCT scans of 2 × 2 × 2 mm^3 cubes L-PBF Ti6Al4V(ELI)-3 at.% Cu CLS, showing (a) the surface view with surface roughness, and (b) cross sectional CT image showing internal microporosity (black voids) and enriched Cu areas (white spots).

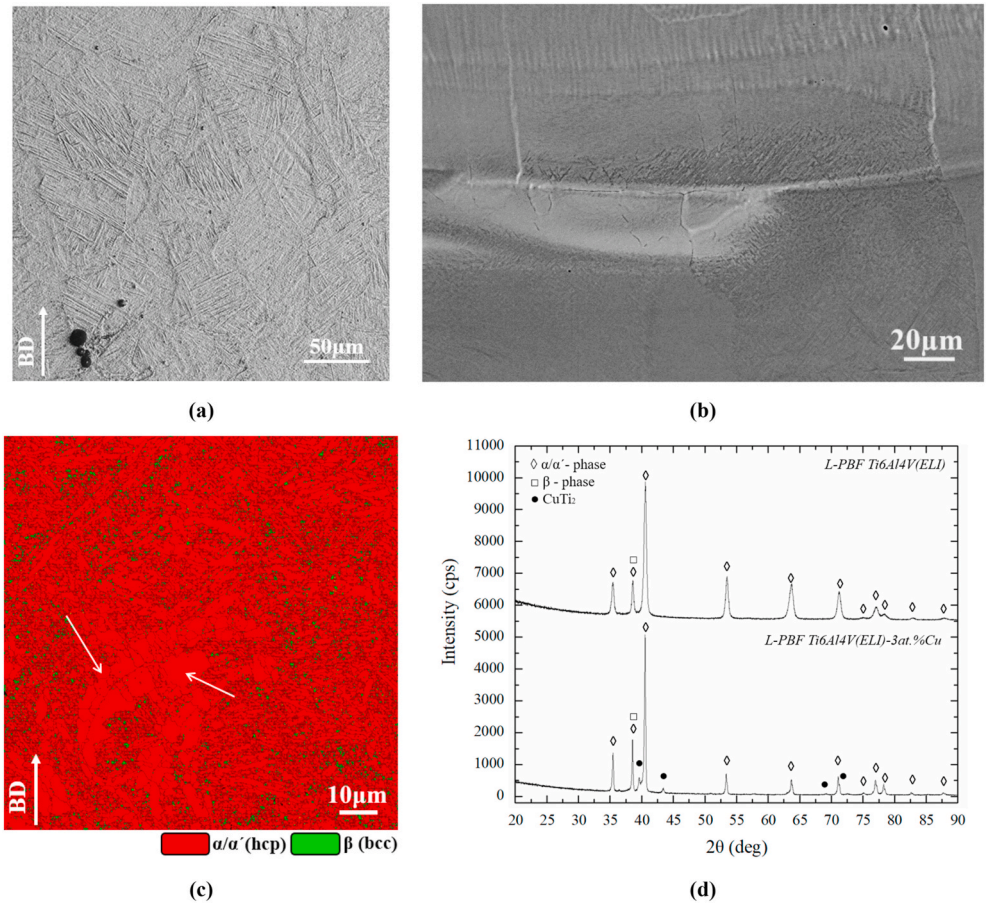

Fig. 4. (a) Optical, (b) SEM micrographs and (c) EBSD mapping of L-PBF Ti6Al4V(ELI)-3 at.% Cu microstructure (rounded α grains indicated with white arrows). (d) Corresponding XRD pattern (together with Ti6Al4V(ELI) one. as reference).

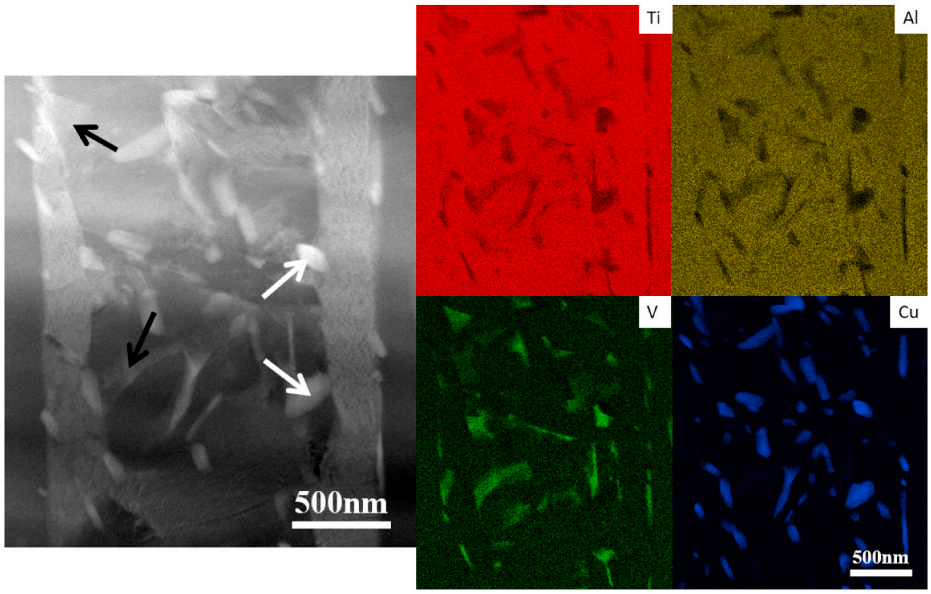

Fig. 5. HR-STEM micrograph and mapping of L-PBF Ti6Al4V(ELI)- 3 at.% Cu material. β-phase precipitates are spotted in vanadium rich areas (black arrows), meanwhile $CuTi_2$ precipitates are spotted in Cu rich areas (white arrows).

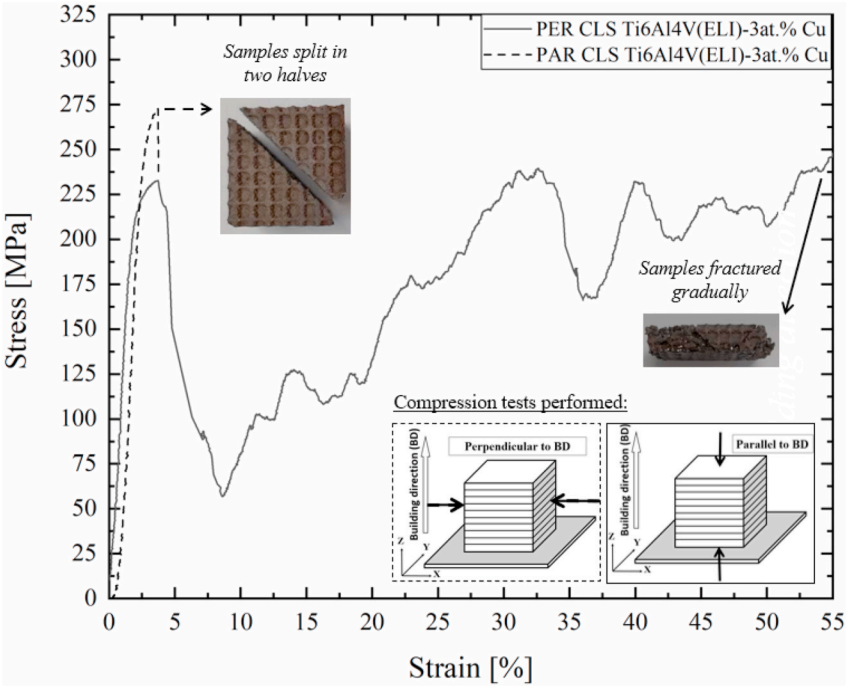

Fig. 6. Compression strain-stress curves of L-PBF Ti6Al4V(ELI)-3 at.% Cu CLS tested perpendicular (continuous line) and parallel (dashed line) to the BD. (For interpretation of the references to colour in this figure legend, the reader is referred to the Web version of this article.)

interface with the α' needles, as well as in connection with the small β-phase.

3.3. Compression testing

Fig. 6 shows the compression stress-strain curves of L-PBF Ti6Al4V (ELI)-3 at.% Cu CLS tested perpendicular and parallel to the BD. In both cases, it was observed a high strength peak followed by a pronounced drop to low-stresses between 5 and 8% strain (Fig. 6). Those peaks were ~28.4% and ~19.4% higher for Ti6Al4V(ELI)-3 at.% Cu with walls oriented perpendicular and parallel to the BD compared to the same L-PBF Ti6Al4V(ELI) CLS (Vilardell et al., 2019). Higher strengths were observed when CLS were tested perpendicular to the BD, 16.4% compared to specimens tested parallel to the BD. Specimens tested perpendicular to the BD showed a complete diagonal shear fracture, dividing the specimen into two halves showing a typical brittle behavior. On the other hand, specimens tested parallel to the BD fractured gradually in diagonal shear fracture by showing load-bearing capacities (K) of about 0.27. The load-bearing capacity was calculated by coefficient K, defined as $K = \frac{\sigma_{min}}{\sigma_b}$, as described in (Zhao et al., 2018), where σ_{min} is the first lowest value of stress after the initial plastic failure and $\sigma_b$is the compression strength. K = 1 and K = 0 is the maximum and the minimum possible load-bearing capacities, respectively.

Table 2 shows the energy absorption, compressive elastic modulus and compression strength values of Ti6Al4V(ELI)-3 at.% Cu CLS, compared to the previously studied L-PBF Ti6Al4V(ELI) CLS. The energy absorption of the CLS was calculated up to the first maximum compressive strength peak, before spit in two halves or started fractured gradually. Differences in energy absorption were found for both tested orientations. L-PBF Ti6Al4V(ELI) – 3 at.% Cu material showed 60–70% lower energy absorption in both directions in comparison with L-PBF Ti6Al4V(ELI). However, CLS tested parallel to the BD showed 21% higher energy absorption for Ti6Al4V(ELI) – 3 at.% Cu CLS.

Compressive elastic modulus and compressive strength were obtained by compression tests perpendicular and parallel to the BD (Table 2). Compressive elastic modulus results showed 39% and 64.5% lower values than the as-designed one, when tested parallel and perpendicular to the BD. Higher compressive elastic modulus was observed for L-PBF Ti6Al4V(ELI)-3 at.% Cu compared to L-PBF Ti6Al4V (ELI) material, 34.6% and 51.5% higher for perpendicular and parallel orientations to the BD, respectively. Ti6Al4V(ELI) −3 at.% Cu specimens tested perpendicular had 13.6% higher stiffness than the ones tested parallel to the BD. Compressive strength results showed the same trend than compressive elastic modulus results. The addition of 3 at.% Cu led increases hardness up to $HV_{0.2}$ 459 ± 7 compared to $HV_{0.2}$ 383 ± 13 from L-PBF Ti6Al4V(ELI) material.

4. Discussion

The properties of CLS depend on different factors, such as material, design and structure (Maconachie et al., 2019). Previously, L-PBF Ti6Al4V(ELI) CLS were topologically optimized with high porosity and a density close to the human bone for biomedical applications (Vilardell et al., 2019). The idea to combine a lattice network to promote osseointegration and reduce stress shielding, plus the addition of bactericidal elements to prevent the risk of bacterial infection is ideal to enhance implant longevity. The addition of Cu into the human body

Table 2
Energy absorption, compressive elastic modulus and compressive strength of L-PBF Ti6Al4V(ELI)-3 at.% Cu and Ti6Al4V(ELI) CLS.

	CLS Ti6Al4V(ELI)-3at.%Cu	CLS Ti6Al4V(ELI) (Vilardell et al., 2019)
Energy absorption [MJ/m^3]		
- *PER to the BD*	4.7 ± 0.8	8.0 ± 1.0
- *PAR to the BD*	5.7 ± 0.3	9.1 ± 0.8
Compressive elastic modulus [GPa]		
- As-designed		27.4
- *PER to BD*	16.7 ± 1.8	12.4 ± 0.9
- *PAR to BD*	14.7 ± 1.0	9.7 ± 1.4
Compressive strength [MPa]		
- *PER to BD*	270.1 ± 3.7	210.3 ± 3.4
- *PAR to BD*	232.1 ± 0.7	194.4 ± 1.4
Vickers hardness [$HV_{0.2}$]	459 ± 7	383 ± 13

should not be harmful as long as is not in large quantities. Copper, as well as iron, calcium and zinc, is an essential nutrient for the body and a trace element vital to the health of all living organisms. Human body cannot form copper by itself and it gets daily from the dietary sources. According to the World Health Organization, 1–3 mg per day of copper are required to prevent any symptoms of deficit (copperalliance.org).

4.1. L-PBF manufacturing

The process parameters, scanning strategy as well as powder and direction of the lattice walls, influence lattice accuracy. Large discrepancies in wall thicknesses by the addition of 3 at.% Cu was due to the lower scanning speed and hatch distance used during L-PBF manufacturing process compared to Ti6Al4V(ELI) material. The higher energy input required for the melting of Ti6Al4V(ELI)-Cu powder mixture, led to larger molten pools, leading to an increase in wall thickness. A similar observation was made in a study of *in-situ* alloying of Ti7.5wt.%Mo and TiTa alloys by L-PBF (Kang et al., 2019; Huang et al., 2020). A higher input energy is required to melt Mo and Ta particles but also to reduce porosity due to the increase in molten pool size. For Ti7.5wt.%Mo alloy, the laser power, hatch distance and layer thickness were fixed at 200 W, 100 mm and 50 mm respectively. The decrease in scanning speed from 1.5 mm/s to 1.0 mm/s led to the increase in relative density from 86.5% to 99.7%, as well as an increase in strain at failure from 1.4% to 9.2% (Kang et al., 2019). In the case of TiTa alloys, for the same scanning parameters, it was observed an increase in porosity with the increase in Ta percentage, being CP Ti = 0.062%, Ti10wt.%Ta = 0.039%, Ti30wt.%Ta = 0.236%, Ti50wt.%Ta = 0.466% (Huang et al., 2020). During the optimization of process parameters of Ti6Al4V-3 at.% Cu, it was found that single tracks had many satellites. The lower scanning speed coupled with the high thermal conductivity of copper and the lower melting point potentially led to this effect. Thus, Ti6Al4V (ELI)- 3 at.% Cu single tracks were more irregular leading to higher surface roughness compared to Ti6Al4V(ELI) single tracks (Vilardell et al., 2020).

4.2. Deformation behavior and failure mechanisms

In general, CLS exhibit stretch- or bending-dominated behavior during compression testing. The deformation behavior mechanism mainly depends on the design and relative density of the CLS, as well as on the material. The type of deformation behavior is connected with the mechanical properties. Briefly, stretch-dominated behavior shows superior strength (e.g for light-weight structural materials) meanwhile bending-dominated shows superior compliance (e.g for dampening or energy absorption) (Bauer et al., 2017; du Plessis et al., 2019). The design of the CLS used in the present study has a stretch-dominated behavior. It is composed of vertical and horizontal walls relative to the build direction. Vertical walls aligned along the loading direction are well known to promote stretch-dominated deformation mechanisms (Mazur et al., 2015; Chen et al., 2019), reaching higher strength and lower energy absorption values compared to bending-dominated lattices. Higher compressive strength peaks followed by a sharp drop in stress were observed in the studied lattices. Deviations in wall thickness strongly influenced such stretch behavior, and as a consequence differences in compressive elastic modulus, strength and energy absorption were found. A higher stretch behavior was observed when thicker walls were placed parallel to the loading direction during compression tests, leading to lower energy absorption compared to thinner walls. Additionally, differences in stretch behavior were also reflected in the failure mechanisms. The increase in thickness of walls aligned along the loading direction led a change in the failure mechanism from gradual failure to split the lattice sample in two halves by diagonal shear failure.

During compressive loading, the development of maximum shear stresses in Ti6Al4V bulk material occurs at an orientation of 45° (Hammer, 2012). The diagonal failure behavior observed in the present study can be perfectly associated with Ti6Al4V(ELI) bulk material due to their high relative density. Other types of failure have been reported by Choy et al. (2017) for cubic and honeycomb CLS depending on their relative density and orientation of the struts with the compression direction. The deformation behavior of cubic and honeycomb lattices shifted from “layer to layer” to “diagonal crack” and from “diagonal shear” to “V-shape” to “diagonal crack” by increasing relative density when vertical struts were parallel and angled to the compression direction.

4.3. Influencing factors on deformation behavior and mechanical properties

Geometrical discrepancies often appear between as-designed and as-manufactured parts for sections reaching the manufacturing limits (Bagheri et al., 2017; Van Bael et al., 2011; Maszybrocka et al., 2019; Ahmed et al., 2019). Walls/struts’ thickness discrepancies increase with the decrease in as-designed struts/wall thicknesses, as well as its orientation with the BD. Vertical thin walls below 0.5 mm showed high distortion, which reduced above ˃0.5 mm (Ahmed et al., 2019). Bagheri et al. (2017) found the highest discrepancies for horizontal struts for a prismatic porous sample obtained by tessellating a tetrahedron-based unit, followed by oblique and vertical struts. In the present study, similar discrepancies in wall thickness were found between the as-designed and as-manufactured CLS, and could be divided in three kinds: (i) the thickening of horizontal walls due to overhanging nature, (ii) the thinning of vertical walls due to scanning strategy and, (iii) general thickening of the walls by the addition of 3 at.% Cu, due to the higher energy input used to melt Ti6Al4V–Cu powder mixture. Because of those wall thickness discrepancies, anisotropy of CLS on mechanical performance was observed when comparing compressive elastic modulus, compressive strength, loading bearing capacity as well as energy absorption values. Lei et al. (2019) employed microCT technique to capture and analyze the geometrical imperfections of L-PBF CLS, and used a finite element modeling method taking the distribution locations of defects into account. The prediction of the results of the reconstructed model were consistent with experimental results as compared to the as-designed and statistical average models. Additionally, in the present study, it was observed that the addition of 3 at.% Cu led to an increase in strength, as well as in hardness, compared to Ti6Al4V(ELI). For the same material, higher strengths were obtained when thicker walls were oriented along the loading direction as expected. However, the alloyed material had higher strength compared to Ti6Al4V(ELI) material for the same orientation (Fig. 7), but lower energy absorption due to the

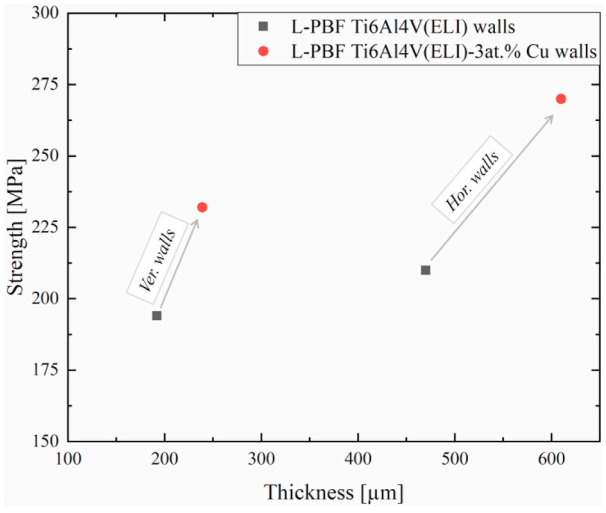

Fig. 7. Relationship between compression strength, wall thickness and alloying material.

increase in strength and stiffness. MicroCT results revealed slightly higher microporosity in Cu alloyed material compared to the standard Ti6Al4V(ELI) specimens. However, this expected reduction in strength is counteracted by the higher influence of the alloying composition. Based on these observations, results showed that alloying is more efficient in strengthening being a factor major than microporosity. Cao et al. (2020) evaluated the role of single geometric defect on the energy absorption in FBCCXYZ CLS and reported that strut thickness variation had a larger impact than strut porosity or strut waviness.

Such observations are supported by TEM and EBSD findings by the formation of intermetallic $CuTi_2$ precipitates and a finer microstructure due to the addition of 3 at.% Cu compared to L-PBF Ti6Al4V(ELI) (Vilardell et al., 2019). However, the increase in strength is at the expense of ductility and energy absorption, as observed experimentally. Similar findings were reported by L-PBF using Ti6Al4V-5 wt.% Cu pre-alloyed powder, resulting in a 40% increase in tensile and yield strengths (Macpherson et al., 2017). The increase in β-phase by the addition of Cu content should not significantly influence the compression strength results, as long as the addition is in very small percentages, in the present case of around ~2% more. Chen et al. (2019) reported hot isostatic pressing (HIP) and heat treatments reduced fracture strength of the struts for L-PBF Ti6Al4V CLS during compression tests due to the decomposition of the α′-phase into α-Widmanstätten and α+β phases, respectively, which are more ductile. Significant changes were especially observed for HIPped CLS, which struts plastically deformed rather than fracturing layer-wise during compression tests. Contrary to L-PBF manufacturing, opposite results were obtained by traditional manufacturing methods. A decrease in tensile strength from 1016 MPa to 387 MPa with an increase in Cu content from 1 to 10% for Ti6Al4V–Cu cast alloy was reported, although 10% Cu alloy showed the highest hardness and the brittleness fracture (Aoki et al., 2004).

5. Conclusions

The present study is focused on the microstructural and mechanical characterization of *in-situ* alloyed Ti6Al4V(ELI)- 3 at.% Cu CLS designed for implant applications. To summarize:

- Discrepancies in wall thickness between the as-designed and the as-manufactured Ti6Al4V(ELI)-3 at.% Cu CLS were found to be due to: (i) the thickening of overhanging horizontal walls, (ii) the thinning of vertical walls due to laser parameters and, (iii) general thickening of the walls (compared to Ti6Al4V(ELI) CLS) due to the addition of 3 at. % Cu content since a higher energy input required to melt the Ti6Al4V–Cu powder mixture.
- The anisotropic nature of the CLS was found to be mostly influenced by discrepancies in wall thicknesses. Higher compressive strength and compressive elastic modulus values, but catastrophic shear failure and hence lower total energy absorption values, were obtained when thicker walls were oriented along the loading direction of the compression tests.
- The addition of 3 at.% Cu content had a higher impact on the compressive strength and compressive elastic modulus of the CLS. Therefore, it led to superior hardness and compressive strength, due the refinement of martensitic phase and formation of $CuTi_2$ intermetallic precipitates compared to Ti6Al4V(ELI) CLS without Cu.
- The increase in the lattices' strength due to the Cu alloying and increase in wall thickness changed the compression failure mode from cracking gradually to catastrophic shear failure.
- The microporosity of the lattice struts increased with the addition of 3 at.% Cu content, but despite this the strength increased.

This approach with the addition of a small quantity of alloying element that has an antibacterial and strengthening effect can be used in all kinds of lattices for implant applications and the rules learned here are not only applicable to topology optimized CLS as demonstrated here. Further work on *in-situ* alloyed CLS for improving fatigue properties of the CLS materials will be undertaken in the future.

Funding

This work supported by the South African Research Chairs Initiative of the Department of Science and Technology and National Research Foundation of South Africa (Grant N⁰ 97994). Authors thank the Swedish Agency for Economic and Regional Growth, Grant No20201144, ATLAB - additive manufacturing laboratory at Karlstad University, and Region Värmland for financial support. Also, authors would like to thank the European Union's horizon 2020 research and innovation programme for the funding received under the ESTEEM3 grant agreement n°823717.

CRediT authorship contribution statement

A.M. Vilardell: Investigation, Validation, Formal analysis, Data curation, Writing - original draft, Writing - review & editing, Visualization, Project administration, Funding acquisition. **A. Takezawa:** Investigation. **A. du Plessis:** Investigation, Resources, Writing - review & editing. **N. Takata:** Investigation, Resources. **P. Krakhmalev:** Conceptualization, Investigation, Validation, Formal analysis, Writing - original draft, Writing - review & editing, Funding acquisition, Project administration. **M. Kobashi:** Resources. **M. Albu:** Investigation, Resources. **G. Kothleitner:** Resources. **I. Yadroitsava:** Conceptualization, Methodology, Writing - review & editing. **I. Yadroitsev:** Conceptualization, Funding acquisition, Resources, Writing - review & editing.

Declaration of competing interest

The authors declare that they have no known competing financial interests or personal relationships that could have appeared to influence the work reported in this paper.

Acknowledgements

Samples were manufactured in CRPM at Central University of Technology, Free State and authors would like to thank Mr. Dean Kouprianoff and Mr. Eric Newby. Additionally, authors would like to thank the Postdoctoral Fellowships for Research in Japan (summer program 2018) from Japan Society for the Promotion of Science (JSPS).

References

Ahmed, A., Majeed, A., Atta, Z., Jia, G., 2019. Dimensional quality and distortion analysis of thin-walled alloy parts of AlSi10Mg manufactured by selective laser melting. JMMP 3, 51.

Aoki, T., Okafor, I.C.I., Watanabe, I., Hattori, M., Oda, Y., Okabe, T., 2004. Mechanical properties of cast Ti-6Al-4V-XCu alloys. J. Oral Rehabil. 31, 1109–1114. https://doi.org/10.1111/j.1365-2842.2004.01347.x.

Bagheri, Z.S., Melancon, D., Liu, L., Johnston, R.B., Pasini, D., 2017. Compensation strategy to reduce geometry and mechanics mismatches in porous biomaterials built with Selective Laser Melting. J Mech Behav Biomed 70, 17–27. https://doi.org/10.1016/j.jmbbm.2016.04.041.

Bauer, J., Meza, L.R., Schaedler, T.A., Schwaiger, R., Zheng, X., Valdevit, L., 2017. Nanolattices: an emerging class of mechanical metamaterials. Adv. Mater. 29, 1701850. https://doi.org/10.1002/adma.201701850.

Cao, X., Jiang, Y., Zhao, T., Wang, P., Wang, Y., Chen, Z., Li, Y., Xiao, D., Fang, D., 2020. Compression experiment and numerical evaluation on mechanical responses of the lattice structures with stochastic geometric defects originated from additive-manufacturing. Compos. B Eng. 194, 108030. https://doi.org/10.1016/j.compositesb.2020.108030.

Chen, J.K., Wu, M.W., Cheng, T.L., Chiang, P.H., 2019. Continuous compression behaviors of selective laser melting Ti-6Al-4V alloy with cuboctahedron cellular structures. Mater. Sci. Eng. C 100, 781–788. https://doi.org/10.1016/j.msec.2019.03.054.

Choy, S.Y., Sun, C.-N., Leong, K.F., Wei, J., 2017. Compressive properties of Ti-6Al-4V lattice structures fabricated by selective laser melting: design, orientation and density. Addit Manuf 16, 213–224. https://doi.org/10.1016/j.addma.2017.06.012.

du Plessis, A., le Roux, S.G., Guelpa, A., 2016. The CT Scanner Facility at Stellenbosch University: an open access X-ray computed tomography laboratory. Nucl. Instrum.

Methods Phys. Res. Sect. B Beam Interact. Mater. Atoms 384, 42–49. https://doi.org/10.1016/j.nimb.2016.08.005.
du Plessis, A., Broeckhoven, C., Yadroitsava, I., Yadroitsev, I., Hands, C.H., Kunju, R., Bhate, D., 2019. Beautiful and functional: a review of biomimetic design in additive manufacturing. Addit Manuf 27, 408–427. https://doi.org/10.1016/j.addma.2019.03.033.
Fischer, M., Joguet, D., Robin, G., Peltier, L., Laheurte, P., 2016. In situ elaboration of a binary Ti–26Nb alloy by selective laser melting of elemental titanium and niobium mixed powders. Mater. Sci. Eng. C 62, 852–859. https://doi.org/10.1016/j.msec.2016.02.033.
Hammer, J.T., 2012. Plastic Deformation and Ductile Fracture of Ti-6Al-4V under Varioius Loading Conditions. The Ohio State University, Degree Master of Science Academic, Department.
https://copperalliance.org.uk/knowledge-base/education/education-resources/copper-essential-human-health/.
Huang, S., Sing, S.L., de Looze, G., Wilson, R., Yeong, W.Y., 2020. Laser powder bed fusion of titanium-tantalum alloys: compositions and designs for biomedical applications. J Mech Behav Biomed Mater 108, 103775. https://doi.org/10.1016/j.jmbbm.2020.103775.
ISSO 13314 - Mechanical testing of metals. Ductility Testing. Compression Test for Porous and Cellular Metals.
Kang, N., Li, Y., Lin, X., Feng, E., Huang, W., 2019. Microstructure and tensile properties of Ti-Mo alloys manufactured via using laser powder bed fusion. J. Alloys Compd. 771, 877–884. https://doi.org/10.1016/j.jallcom.2018.09.008.
Krakhmalev, P., Yadroitsev, I., Yadroitsava, I., de Smidt, O., 2017. Functionalization of biomedical Ti6Al4V via in situ alloying by Cu during laser powder bed fusion manufacturing. Materials 10, 1154. https://doi.org/10.3390/ma10101154.
Lei, H., Li, C., Meng, J., Zhou, H., Liu, Y., Zhang, X., Wang, P., Fang, D., 2019. Evaluation of compressive properties of SLM-fabricated multi-layer lattice structures by experimental test and μ-CT-based finite element analysis. Mater. Des. 169, 107685. https://doi.org/10.1016/j.matdes.2019.107685.
Li, G., Wang, L., Pan, W., Yang, F., Jiang, W., Wu, X., Kong, X., Dai, K., Hao, Y., 2016. In vitro and in vivo study of additive manufactured porous Ti6Al4V scaffolds for repairing bone defects. Sci. Rep. 6 https://doi.org/10.1038/srep34072.
Liu, J., Li, F., Liu, C., Wang, H., Ren, B., Yang, K., Zhang, E., 2014. Effect of Cu content on the antibacterial activity of titanium–copper sintered alloys. Mater. Sci. Eng. C 35, 392–400. https://doi.org/10.1016/j.msec.2013.11.028.
Maconachie, T., Leary, M., Lozanovski, B., Zhang, X., Qian, M., Faruque, O., Brandt, M., 2019. SLM lattice structures: properties, performance, applications and challenges. Mater. Des. 183, 108137. https://doi.org/10.1016/j.matdes.2019.108137.
Macpherson, A., Li, X., McCormick, P., Ren, L., Yang, K., Sercombe, T.B., 2017. Antibacterial titanium produced using selective laser melting. J. Occup. Med. 69, 2719–2724. https://doi.org/10.1007/s11837-017-2589-y.
Maietta, S., Gloria, A., Improta, G., Richetta, M., De Santis, R., Martorelli, M., 2019. A further analysis on Ti6Al4V lattice structures manufactured by selective laser melting. J Healthc Eng 1–9. https://doi.org/10.1155/2019/3212594, 2019.
Maszybrocka, J., Gapiński, B., Dworak, M., Skrabalak, G., Stwora, A., 2019. The manufacturability and compression properties of the Schwarz Diamond type Ti6Al4V cellular lattice fabricated by selective laser melting. Int. J. Adv. Manuf. Technol. 105, 3411–3425. https://doi.org/10.1007/s00170-019-04422-6.
Mazur, M., Leary, M., Sun, S., Vcelka, M., Shidid, D., Brandt, M., 2015. Deformation and failure behaviour of Ti-6Al-4V lattice structures manufactured by selective laser melting (SLM). Int. J. Adv. Manuf. Technol. https://doi.org/10.1007/s00170-015-7655-4.
Onal, E., Frith, J., Jurg, M., Wu, X., Molotnikov, A., 2018. Mechanical properties and in vitro behavior of additively manufactured and functionally graded Ti6Al4V porous scaffolds. Metals 8, 200. https://doi.org/10.3390/met8040200.
Peng, C., Liu, Y., Liu, H., Zhang, S., Bai, C., Wan, Y., Ren, L., Yang, K., 2019. Optimization of annealing treatment and comprehensive properties of Cu-containing Ti6Al4V-xCu alloys. J. Mater. Sci. Technol. 35, 2121–2131. https://doi.org/10.1016/j.jmst.2019.05.020.
Ren, L., Ma, Z., Li, M., Zhang, Y., Liu, W., Liao, Z., Yang, K., 2014. Antibacterial properties of Ti–6Al–4V–xCu alloys. J. Mater. Sci. Technol. 30, 699–705. https://doi.org/10.1016/j.jmst.2013.12.014.
Sallica-Leva, E., Caram, R., Jardini, A.L., Fogagnolo, J.B., 2016. Ductility improvement due to martensite α′ decomposition in porous Ti–6Al–4V parts produced by selective laser melting for orthopedic implants. J Mech Behav Biomed 54, 149–158. https://doi.org/10.1016/j.jmbbm.2015.09.020.
Schlossmacher, P., Klenov, D.O., Freitag, B., von Harrach, H.S., 2010. Enhanced detection sensitivity with a new windowless XEDS system for AEM based on silicon drift detector technology. Micros. Today. 18, 14–20.
Song, Z., Borgwardt, L., Høiby, N., Wu, H., Sørensen, T.S., Borgwardt, A., 2013. Prosthesis infections after orthopedic joint replacement: the possible role of bacterial biofilms. Orthop. Rev. 5, 14. https://doi.org/10.4081/or.2013.e14.
Van Bael, S., Kerckhofs, G., Moesen, M., Pyka, G., Schrooten, J., Kruth, J.P., 2011. Micro-CT-based improvement of geometrical and mechanical controllability of selective laser melted Ti6Al4V porous structures. Mater. Sci. Eng., A 528, 7423–7431. https://doi.org/10.1016/j.msea.2011.06.045.
Vilardell, A.M., Takezawa, A., du Plessis, A., Takata, N., Krakhmalev, P., Kobashi, M., Yadroitsava, I., Yadroitsev, I., 2019. Topology optimization and characterization of Ti6Al4V ELI cellular lattice structures by laser powder bed fusion for biomedical applications. Mater. Sci. Eng. 766, 138330. https://doi.org/10.1016/j.msea.2019.138330.
Vilardell, A.M., Yadroitsev, I., Yadroitsava, I., Albu, M., Takata, N., Kobashi, M., Krakhmalev, P., Kouprianoff, D., Kothleitner, G., du Plessis, A., 2020. Manufacturing and characterization of in-situ alloyed Ti6Al4V(ELI)-3 at.% Cu by laser powder bed fusion. Addit Manuf 36, 101436. https://doi.org/10.1016/j.addma.2020.101436.
Xu, W., Brandt, M., Sun, S., Elambasseril, J., Liu, Q., Latham, K., Xia, K., Qian, M., 2015. Additive manufacturing of strong and ductile Ti–6Al–4V by selective laser melting via in situ martensite decomposition. Acta Mater. 85, 74–84. https://doi.org/10.1016/j.actamat.2014.11.028.
Xu, Y., Zhang, D., Hu, S., Chen, R., Gu, Y., Kong, X., Tao, J., Jiang, Y., 2019. Mechanical properties tailoring of topology optimized and selective laser melting fabricated Ti6Al4V lattice structure. J Mech Behav Biomed Mater 99, 225–239. https://doi.org/10.1016/j.jmbbm.2019.06.021.
Yánez, A., Herrera, A., Martel, O., Monopoli, D., Afonso, H., 2016. Compressive behaviour of gyroid lattice structures for human cancellous bone implant applications. Mater. Sci. Eng. C 68, 445–448. https://doi.org/10.1016/j.msec.2016.06.016.
Zhang, X.-Y., Fang, G., Leeflang, S., Zadpoor, A.A., Zhou, J., 2019. Topological design, permeability and mechanical behavior of additively manufactured functionally graded porous metallic biomaterials. Acta Biomater. 84, 437–452. https://doi.org/10.1016/j.actbio.2018.12.013.
Zhao, M., Liu, F., Fu, G., Zhang, D., Zhang, T., Zhou, H., 2018. Improved mechanical properties and energy absorption of BCC lattice structures with triply periodic minimal surfaces fabricated by SLM. Materials 11, 2411. https://doi.org/10.3390/ma11122411.